SSRG International Journal of Electrical and Electronics Engineering
ISSN: 2348-8379/ https://doi.org/10.14445/23488379/IJEEE-V12I4P107

Volume 12 Issue 4, 102-120, April 2025

Original Article

Intelligent Energy Management System for PV-Fuel Cell Powered BLDC-EVS with High-Gain Landsman Converter and RBFNN MPPT Control

Killamsetti Vijetha[1*], D. Srinivasa Rao[2]

[1,2]*Department of Computer Science and Engineering, Medicaps University, Indore, Madhya Pradesh, India.*

[1]*Corresponding Author : vijetha258@gmail.com*

Received: 04 February 2025 Revised: 06 March 2025 Accepted: 08 April 2025 Published: 29 April 2025

Abstract- *Sustainable Transportation possesses various limitations; hence, integrating an Energy Management System (EMS) provides significant solutions for Electric Vehicle (EV). This innovative system incorporates a Photovoltaic (PV) system and Fuel Cell (FC) within the Hybrid Renewable Energy System (HRES) to provide enhanced power supply to the Brushless DC (BLDC) motor. The Radial Basis Function Neural Network (RBFNN) is integrated with a PV system for Maximum Power Point Tracking (MPPT) to attain improved energy management, assuring effective PV performance under varying environmental conditions. In addition, the Landsman Converter is utilized to attain efficient power regulation and conversion between PV and the EV DC bus. Furthermore, FC augments the system's performance by providing continuous power. Additionally, implementing a battery and a super-capacitor ensures improved energy storage and retrieval. Thus, the overall system contributes increased power stability during peak load demands, regenerative braking and fluctuations, enhancing the system performance in terms of efficiency and reliability. The Landsman converter attains a gain of 1:10 with an overall efficiency of 98%. Therefore, the innovation of intelligent EMS attains improved range, performance, and dependability of EVs, indicating a significant improvement in the adoption of renewable energy-powered transportation. The proposed system is implemented using MATLAB Simulink to showcase its effectiveness.*

Keywords - *EMS, PV, FC, BLDC motor, RBFNN, MPPT, Landsman converter, Super-capacitor, Bi-directional buck-boost converter, Battery.*

1. Introduction

In recent times, due to the increasing demand and expenses for fuels, seeking to attain sustainable vehicle propulsion is mandatory [1, 2]. Thus, to attain improved energy conservation and reduced pollution, EVs are developed as they attain higher performance efficacy with limited carbon emission [3]. However, motors play an essential part in further enhancing EV performance as motor efficiency significantly impacts EV functioning [4]. There are several motors in consideration, such as Permanent Magnet Synchronous Motor (PMSM) [5], PMBLDC [6] and Switched Reluctance Motor (SRM) [7]. These motors provide higher power density with simpler, cost-effective installation and faster dynamic responses. Nevertheless, these approaches also produce increased noises, losses and higher torque ripples [8].

Table 1. Advantages of using BLDC motor over brushed motor

Characteristics	Brushed Motor	Brushless DC Motor
Efficiency	Reduced efficiency due to energy losses caused by friction and heat generation	Increased efficiency as there are no brushes to produce friction and heat.
Torque	Moderate torque with significant losses due to friction	Higher torque
Speed	Minimal operating speed	Capable of operating at high speed with stable performance
Noise	Higher noise generation	Less or little noise is produced
Motor Lifespan	Limited motor lifespan	Longer lifespan
Maintenance	Requires consistent maintenance	Requires minimal maintenance

Table 1 states the benefits of using a Brushless DC motor instead of a brushed motor, considering the drawbacks of utilizing a brushed motor brushless DC motor are vitally regarded. Henceforth, to attain the desired level of EV performance, a BLDC motor is utilized to ensure improved motor efficacy in terms of producing reduced losses, noises, and ripples. Significantly, BLDC motors possess a higher lifespan when compared to the above-mentioned conventional motors. Anyway, the performance of BLDC motors relies heavily on regulated power sources [9, 10]. Consecutively, to meet the power requirements of the BLDC motors, various Renewable Energy Sources (RES) are considered, such as PV, FC, wind energy, Hydro-power and geothermal energy, due to their ability to provide clean, sustainable and less polluted energy by reducing the carbon emission [11]. Among which PV and FC are widely utilized due to their unlimited, scalable and minimized implementation expenses. The hybridization of PV and FC within HRES ensures enhanced energy reliability by delivering a consistent and sustainable power supply. However, the output of PV panels exhibits fluctuations with varying temperatures, leading to inconsistent power delivery and affecting the motor's smoother operation.

Also, FCs take time to respond to load variations, hence failing to provide instantaneous power changes [12]. Initially, the output voltage produced by the PV system is less; thus, converters are considered essential to boost PV production. Conventional converters, including Cuk [13], Boost [14], SEPIC [15], and KSK [16] converters, perform better functioning by boosting PV production by stepping up the low voltage level to high voltage levels. However, these converters struggle with certain limitations, including reduced efficiency, increased complexity and switching losses. Thus, to overcome these limitations, a Landsman Converter is proposed, which attains high voltage gain and higher power density with reduced ripple, noises, and component count.

To further track, monitor, control and extract maximum power from PV, various MPPT algorithms are taken into consideration, such as Artificial Neural Network (ANN) [17], Feed-Forward Neural Network (FFNN) [18] and Adaptive Network-Based Fuzzy Inference System (BRBFNN) [19] as they offer enhanced problem ability with increased uncertainty handling during varying environmental conditions along with making them more convenient in terms of identifying intricate patterns, prediction and control. However, their performance efficacy completely depends upon factors like quality and quantity of data along with adequate parameter tuning. Also, these algorithms may fall into suboptimal solutions due to the occurrence of sudden drops or increases in solar irradiance.

2. Literature Survey

In [20], a soft-switching interleaved boost converter is suggested for charging EVs that offers enhanced dependability, high efficiency and multiphase configuration support, and integration with a range of power sources, including RES, batteries and grids. Although it improves performance and lowers switching losses, it also increases complexity, raises initial costs and makes precise control difficult to maintain. The work in [21] has presented a converter for EVs that allows for the flexible integration of battery and solar PV sources and has dual voltage outputs for different loads. It provides a straightforward, economical design with less distortion and effective energy management. However, the drawbacks include complicated control in dynamic situations, limited scalability and possible voltage spikes.

In [22], a technique for managing and sizing prosumers' energy systems is introduced that combines battery storage, bidirectional EV chargers, and PV panels. The proposed approach provides significant cost reductions, effective battery use, and increased dependability. However, it also has drawbacks, such as complexity, high start-up costs, computational demands, and battery degradation uncertainties. The method in [23] has focused on increasing reliability through Vehicle-to-Grid (V2G) technology. It offers a strategy for best integrating solar PV rooftop units with electric vehicle charging stations. The advantages of EV charging include increased system dependability and less detrimental effects on the grid, while the disadvantages include possible problems that could compromise the overall effectiveness and dependability of the system.

In [24], a Flexible Printed Circuit Board (FPCB) layered shield structure is proposed to lower shaft voltage in BLDC motors for EVs. By preventing shaft voltage-related faults and bearing damage, the technique greatly improves durability, reliability and safety. However, issues still exist because of manufacturing complexity, sensitivity to mechanical and thermal stresses, and susceptibility to shaft voltage from high-frequency switching, which affect overall performance and maintenance.

On the whole, amidst the advancements in EV technology, numerous issues exist in attaining improved performance and efficiency. Although BLDC motors provide enhanced efficiency and lifespan compared to conventional motors, their integration with EVs requires a regulated power supply. Also, the intermittent nature of renewable sources poses challenges in maintaining reliable power flow. Moreover, conventional converters exhibit limitations like reduced efficiency and restricted voltage boost. When considering MPPT approaches, they struggle with environmental variations that demand improved accuracy and adaptability.

To address these gaps, the proposed model is developed using a Landsman converter with RBFNN-based MPPT control, which achieves increased tracking capabilities with rapid convergence and achieves an enhanced PV performance control system. In addition to this, a battery and a super-capacitor are deployed to ensure increased energy storage with proper redemption using a bi-directional Buck-Boost converter. Therefore, the overall proposed system, together with the deployment of advanced components, ensures improved energy management with better performance for PV-FC-powered BLDC-EV systems. The major outline and novel contributions of the proposed system are listed below,

- To integrate Hybrid Renewable Energy Resources (HRES) based PV and FC to provide consistent and sustainable power supply to the BLDC motor-driven EV.
- To ensure proper and improved energy management within the PV system, an RBFNN-based MPPT control approach is implemented.
- To regulate the PV power generation, a Landsman converter is utilized which attains increased voltage gain with reduced losses.
- To ensure enhanced energy storage, a battery and a super-capacitor are deployed through a Bi-directional Buck-Boost converter, enabling better storage and retrieval.

3. Proposed System

Figure 1 represents the block diagram of the proposed energy management system for PV-FC powered BLDC motor-driven EV. The process begins with a PV system, which produces solar power to meet the energy requirements of BLDC-driven EVs. However, the PV system initially generates low voltage output; hence, the landsman converter is deployed to the PV system to regulate the PV output voltage. Integrating the Landsman converter provides an appropriate voltage level for the DC bus. For which the desired switching pulses are given using the PWM generator. The output voltage obtained from the converter is now processed using the RBFNN-MPPT controller. Implementing the RBFNN-MPPT controller provides enhanced PV production control, accurate tracking, and better adaptability to varying environmental conditions.

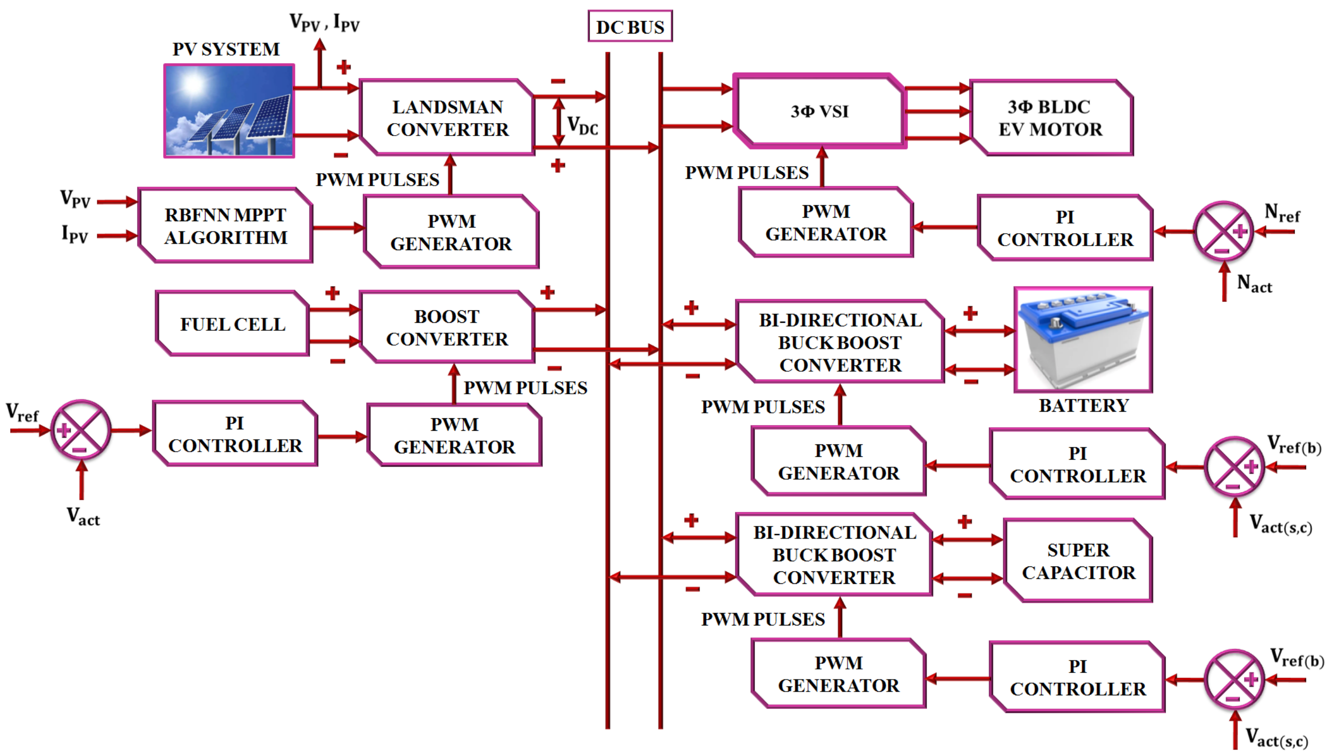

Fig. 1 Proposed system block diagram

In addition to the PV system, FC also generates power that is maintained using a boost converter which is used to step up voltage level. Boost converter output is further regulated using the PI controller, ensuring stabilized power delivery from the FC. Later, the power produced from PV and FC passes through the common DC bus, which is also shared by a battery and a super-capacitor. Power from the DC bus flows to the EV driven using the BLDC motor through a three-phase VSI, which converts the DC supply to AC. Additionally, the excess energy generated is fed to the battery and super-capacitor, enabling better energy storage and retrieval. These storage units are further controlled using the PI controllers to stabilize the voltage levels.

Therefore, the overall proposed model integrating HRES, efficient energy storage units and an enhanced power control approach ensures a consistent and reliable power supply with improved performance and control management.

3.1. PV System

To develop the desired PV module with the necessary current and voltage, a large number of solar cell units are used. The current collecting bus, contacts, and metal grid losses are indicated by the R_S series resistance, whereas the flow of a small leakage current through the parallel path losses is described by the R_P parallel resistance. The PV cell output current I_{pv} is expressed utilizing (1), and the circuit of PV is shown in Figure 2.

$$I_{pv(cell)} = I_{ph} - I_s\left(exp\left(\frac{V_{pv}+I_{pv}\times R_S}{V_t}\right)-1\right)-\frac{(V_{pv}+I_{pv}\times R_S)}{R_P} \tag{1}$$

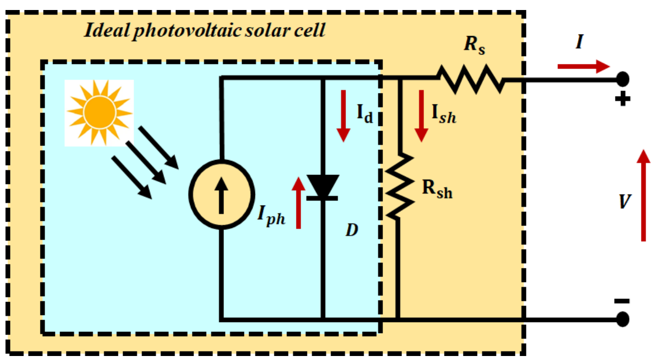

Fig. 2 Circuit diagram of PV system

PV panel is essentially generated by connecting many solar PV cells in series $(N_s)$and parallel (N_p). Consequently, the PV module's output current is expressed as,

$$I_{pv(module)} = N_p \times I_{ph} - N_p \times I_s\left[exp\left(\frac{V_{pv}+I_{pv}\times R_S}{N_S\times V_t}\right)-1\right]-N_p\times\frac{V_{pv}+I_{pv}\times R_S}{N_S\times R_P} \tag{2}$$

$$V_t = \frac{A\times K\times T}{q} \tag{3}$$

Where V_t is the PV cell's thermal voltage. A PV module's output $P-V$ and $I-V$ characteristics exhibit discernible changes when subjected to varying environmental circumstances, particularly for different solar irradiation. Subsequently, the voltage of the PV system is improved by utilizing a Landsman converter.

3.2. Modelling of Landsman Converter

Landsman converter function in CCM regardless of changes in the amount of irradiance, as displayed in Figure 3. Input and output voltage are denoted using V_{pv}andV_O. The switch is indicated using$S$, and output resistance is represented as R.

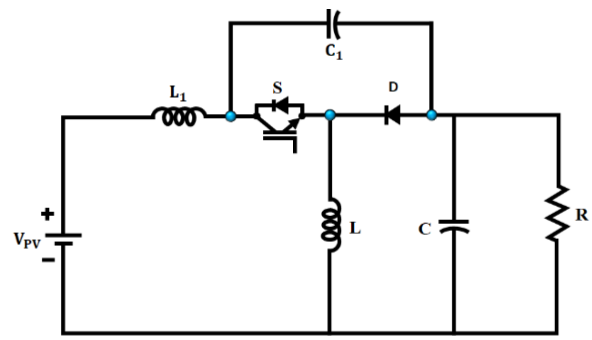

Fig. 3 Circuit diagram of landsman converter

3.2.1. Mode 1

The circuit configuration seen in Figure 4 is the consequence of the voltage across an intermediate capacitor C_1 reverse biasing the diode when the switch is active. The switch is traversed by the inductor current (i_L). Energy is provided to L, and the output whenC_1 discharges through the switch because V_{C1} is greater than the output voltage V_{dc}. Consequently, as Figure 4 demonstrates,i_L increases and V_{C1} decreases. The input inductor L_1receives energy from the input.

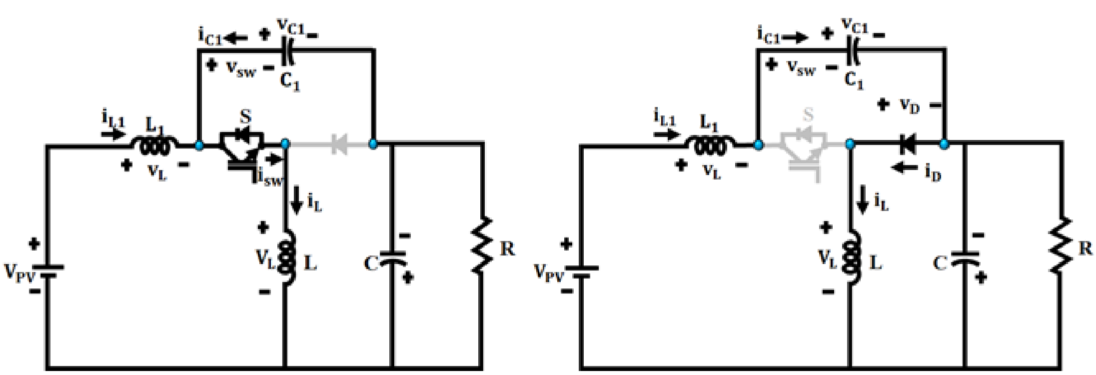

Fig. 4 Modes of developed converter

3.2.2. Mode 2

In this stage, the diode is forward-biased when the switch is off. Diode is traversed byi_L. Through the diode, the inductor L converts its stored energy to output. Conversely, energy from both the input and L_1charges C_1through the diode. Assuming that every ripple component in i_{L1} flows via C_1. An extra flux $\Delta\Phi$ is shown by the shaded region in the V_{C1} waveform. Consequently, the peak-to-peak current ripple ΔI_{L1} is,

$$\Delta I_{L1} = \frac{\Delta\Phi}{L_1} = \frac{1}{L_1}\frac{1}{2}\frac{\Delta V_{C1}}{2}\frac{T}{2} \tag{4}$$

When the switch is inactive, the current via C_1 is,

$$i_{C1} = I_{L1} = C_1\frac{\Delta V_{C1}}{(1-D)T} \tag{5}$$

Where T is the switching period, and D is the duty ratio. The voltage ripple content in V_{C1} is calculated as,

$$\Delta V_{C1} = \frac{I_{L1}}{C_1}(1-D)T \tag{6}$$

Substituting ΔV_{C1} from (6) into (4) gives,

$$\Delta I_{L1} = \frac{1}{L_1}\frac{1}{2}\frac{I_{L1}}{2C_1}(1-D)T\frac{T}{2} \tag{7}$$

$$\Delta I_{L1} = \frac{1}{8L_1C_1}\frac{I_{L1}(1-D)}{f_{SW}^2} \tag{8}$$

$$\frac{\Delta I_{L1}}{I_{L1}} = \frac{1}{8L_1C_1}\frac{(1-D)}{f_{SW}^2} \tag{9}$$

Where the switching frequency is denoted by $f_{SW} = {}^{1}/_{T}$. From the input-output relationship,

$$I_{L1} = \frac{D}{1-D}I_{dc} \tag{10}$$

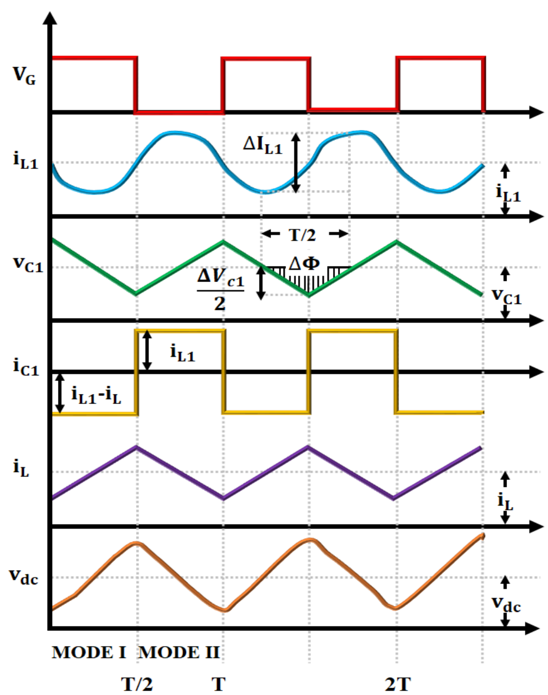

Fig. 5 Functional waveform of developed converter

Where I_{dc} is Landsman converter output current. Thus, substituting I_{L1} from expression (10) into (8),

$$L_1 = \frac{DI_{dc}}{8f_{SW}^2C_1\Delta I_{L1}} \tag{11}$$

Figure 5 reveals the functional waveform of the developed converter.

3.3. Modelling of RBFNN-MPPT

RBFNN was selected for MPPT due to its abilities, such as superior speed, accuracy, and adaptability. When compared to conventional approaches, RBFNN integrates self-learning and pattern recognition abilities for predicting MPP in an accurate manner. It also exhibits faster training and improved generalization ability.

Also, it has the tendency to adapt to variations because of localized learning characteristics quickly. RBFNN-MPPT architecture is shown in Figure 6, which consists of a hidden layer, input layer and output layer, which enables PV to extract maximum power along with accurate MPP tracking. This process is accomplished using the multi-layer activation functions, which are trained using a supervised learning approach. The RBFNN-MPPT approach fine-tunes its weights to produce the predicted output when a certain set of inputs is supplied.

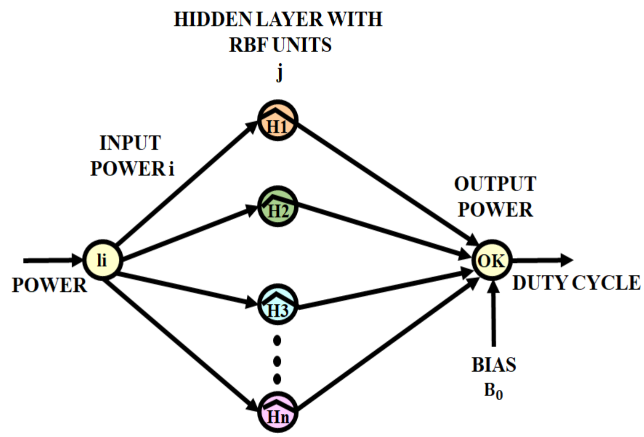

Fig. 6 Structure of RBFNN-based MPPT

The input layer considers the measured PV power and the converter duty cycle inputs. Without any modifications, these inputs are transmitted to the hidden layer, the core computational layer of RBFNN, which features special activation functions.

RBFNN is an activation function with a shorter distance from function establishments. A Gaussian activation function focused on a vector integrates with a hidden layer, which does not have any additional weights. The response of the function relies only on the distance from the center. The j^{th} Gaussian hidden unit receives input directly.

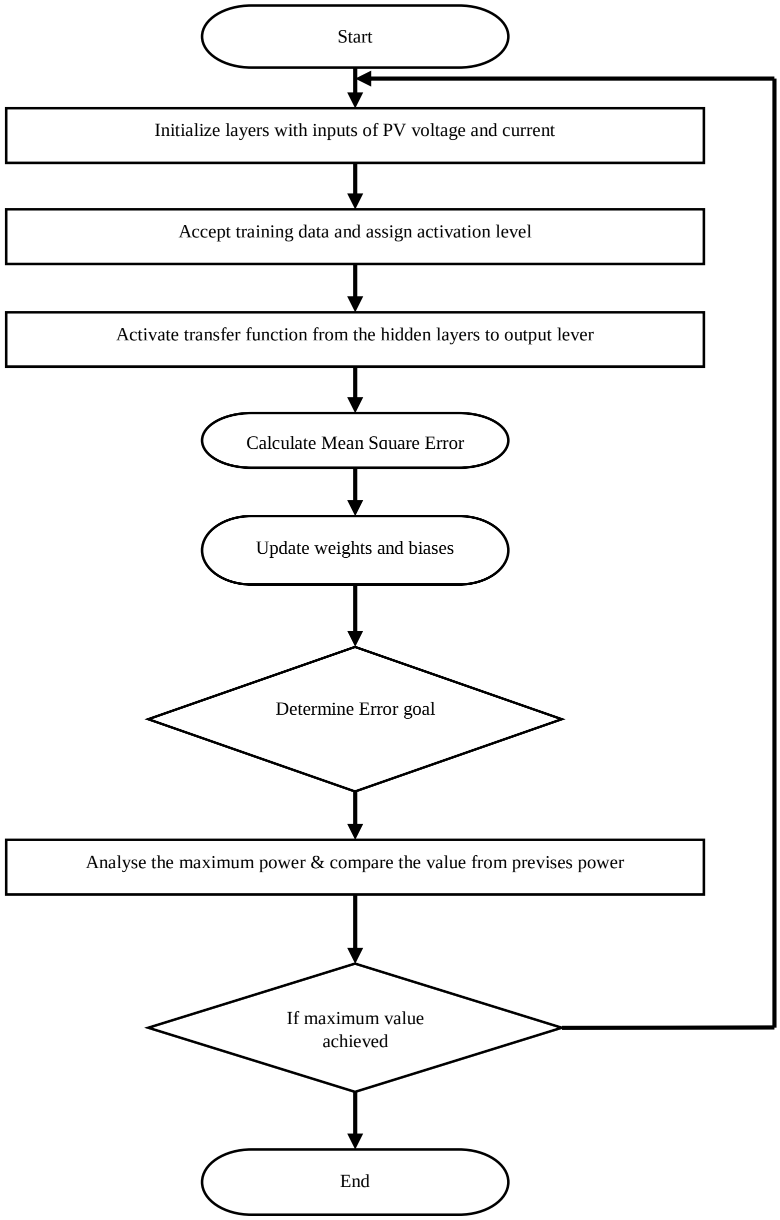

Fig. 7 Flowchart of RBFNN based MPPT

The Euclidean distance is calculated by each hidden neuron, and the related output is given by,

$$H_j = \exp - \frac{\|X - C_j\|^2}{2\sigma_j^2} \tag{12}$$

Here, σ_j^2-spread parameter, C_j-center vector, X-input feature vector.Output of the RBF's k^{th} unit is,

$$O_k = B_o + \sum_{j=1}^{h} W_{jk} * H_j \tag{13}$$

Here, O_k-final output, B_o-bias term, W_{jk}-weight. The output layer determines the converter's optimal duty cycle which in turn ensures the extraction of maximum power. Figure 7 represents the flowchart of RBFNN-based MPPT. Where H_j denotes the j^{th} hidden unit's radial basis output and$H_j = f\left(\|I - c_j\|\right)$. Here, $c \in R$ indicates the RBF's centre with radius r.

$$f(x) = e^{\left(\frac{\|I_i - c_j\|^2}{r^2}\right)} \tag{14}$$

Using supervised learning, the network is trained in which the irradiance values are mapped corresponding to the duty cycle and PV power. After training, the optimal duty cycle is predicted by RBENN, and the network adjusts dynamically to environmental fluctuations with the rapid recalculation of outputs, which depends on new input conditions. This research utilizes another RES named Fuel Cell to improve the efficacy of an overall system.

3.4. Fuel Cell-Based Boost Converter

An FC is a static energy conversion device that directly transforms fuel chemical reactions into electrical energy with a small amount of heat and water as a by-product. FCs make it easier to convert hydrogen and oxygen into power and water than thermal or electromechanical processes. The fuel cell's anode and cathode go through particular reactions when exposed to an electric field, as seen in Figure 8. Once equilibrium has been reached, the ions migrate across the electrodes.

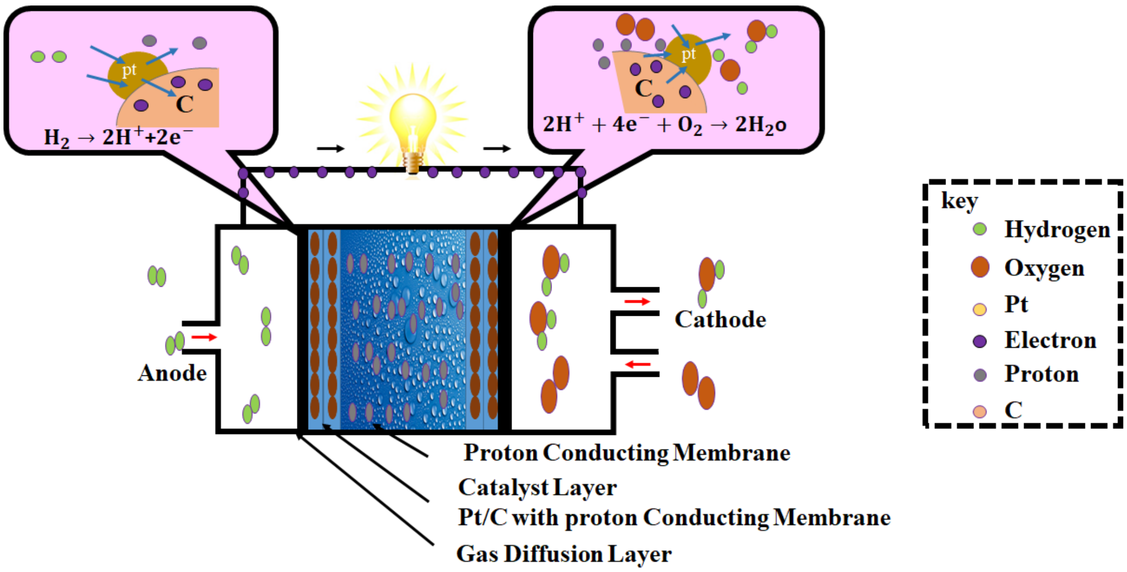

Fig. 8 Operation diagram of FC

The oxidation and reduction reactions take place at the anode and cathode of the Fuel Cell (FC). Water is produced at the cathode by combining two protons and electrons, while at the anode, hydrogen oxidation occurs to yield protons and electrons. The total chemical reaction is,

$$H_2 + \frac{1}{2}O_2 \longrightarrow 2H_2\,O + electrical\ energy + heat\ energy \quad (15)$$

The voltage produced from the FC is

$$V_{FC} = E_{nernst} - V_{act} - V_{ohmic} - V_{con} \quad (16)$$

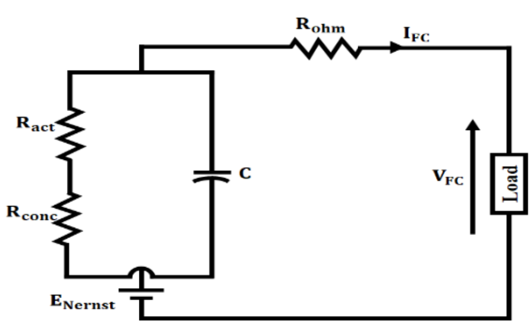

Fig. 9 Equivalent circuit of FC

Where V_{act} is exploited for modeling the activation losses that are expressed as,

$$V_{act} = A\ ln\left(\frac{i_{FC}+i_n}{i_0}\right) \quad (17)$$

The voltage drop because of Ohmic losses is,

$$V_{ohmic} = R_m(i_{FC} + i_n) \quad (18)$$

The concentration losses are,

$$V_{con} = -B\ ln\left(1 - \frac{i_{FC}+i_n}{i_1}\right) \quad (19)$$

Figure 9 depicts the equivalent circuit of the FC. The low voltage of FC is improved with the aid of a boost converter, as revealed in Figure 10. Two basic modes of operation for the boost converter are shown in Figure 11. The transistor switch is closed, and the diode switch is open in the ON state(t_{ON}).

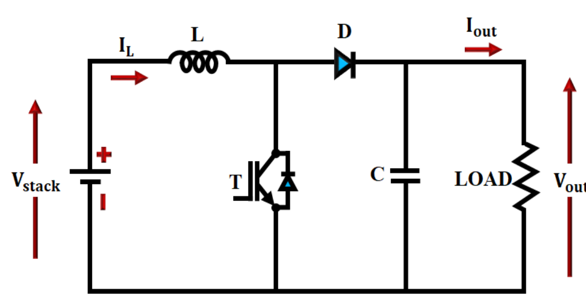

Fig. 10 Boost converter

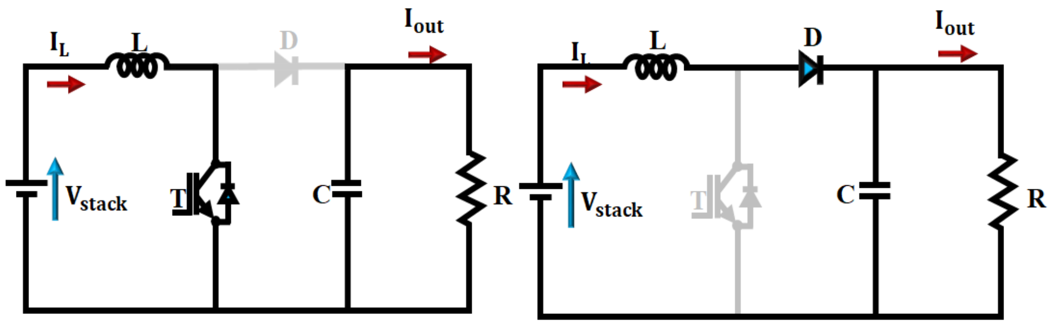

Fig. 11 Stages of boost converter

For energy storage, the inductor is linked to the source voltage. The expressions for this stage are,

$$\frac{di_L}{dt} = \frac{1}{L}(V_{stack}) \tag{20}$$

$$\frac{dV_{out}}{dt} = \frac{1}{C}(-i_{out}) \tag{21}$$

As a result, the output filtering capacitor C and the resistance R is linked to the inductor. The expressions for the second stage are,

$$\frac{di_L}{dt} = \frac{1}{L}(V_{stack} - V_{out}) \tag{22}$$

$$\frac{dV_{out}}{dt} = \frac{1}{C}(i_L - i_{out}) \tag{23}$$

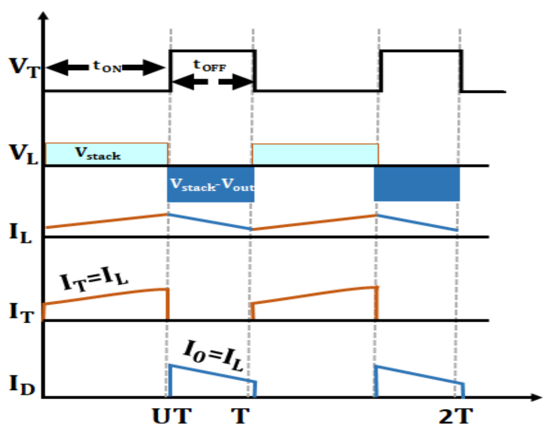

Fig. 12 Functional waveform of boost converter

The voltage gain of the boost converter is,

$$\frac{V_{out}}{V_{stack}} = \left(\frac{1}{1-u}\right) \tag{24}$$

Figure 12 depicts the functional waveform of the boost converter. Where u is a duty cycle. Then, the obtained AC voltage from VSI is given to the 3ϕBLDC motor for EV charging.

3.5. Modelling of 3ϕ BLDC Motor

The configuration of the BLDC motor is presented in Figure 13. BLDC motor normally contains null brushes, and the motor operation is performed using the particular rotor position. BLDC motor is developed utilizing the permanent magnet that is fixed onto the rotor, and the BLDC winding is evaluated using,

$$V_a = I_a R_a + L\frac{di_a}{dt} + e_a \tag{25}$$

$$V_b = I_b R_b + L\frac{di_b}{dt} + e_b \tag{26}$$

$$V_c = I_c R_c + L\frac{di_c}{dt} + e_c \tag{27}$$

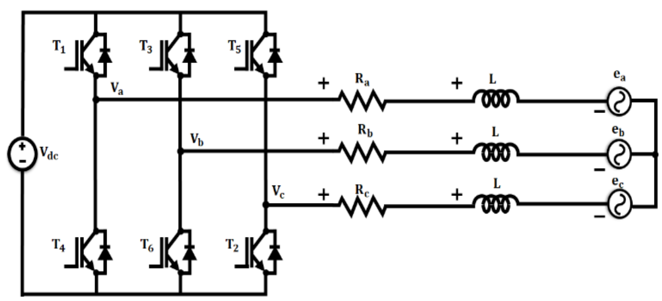

Fig. 13 Equivalent circuit of BLDC motor

The mechanical time constant is,

$$\tau_m = \frac{RJ}{K_e K_t} \tag{28}$$

The electrical time constant is,

$$\tau_e = \frac{L}{3R} \tag{29}$$

$$K_E = \frac{3RJ}{K_T \tau_M} \tag{30}$$

The BLDC motor's transfer function equation is,

$$G(S) = \frac{\omega_m}{V_s} = \frac{1/K_e}{\tau_m \tau_e s^2 + \tau_m s + 1} \tag{31}$$

After that, a Bidirectional buck-boost converter is utilized for charging and discharging operations for both battery and supercapacitor.

3.6. Bidirectional Buck-Boost Converter

As illustrated in Figure 14, a bidirectional buck-boost converter attains power reversibility via its switches, which effectively transmit current in both directions. This leads to two different modes of operation.

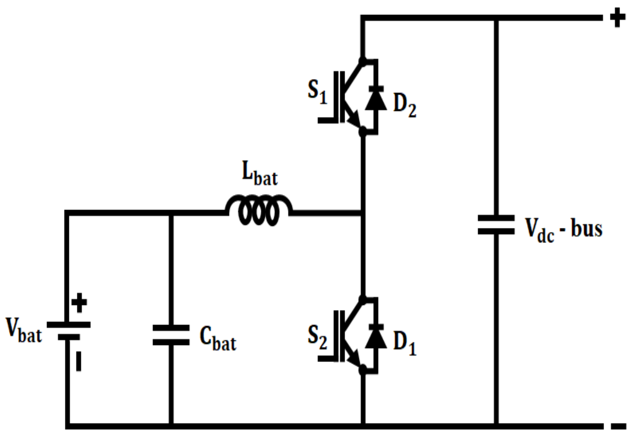

Fig. 14 Structure of bidirectional buck-boost converter

3.6.1. Buck Mode

A bidirectional converter acts as a buck converter when the battery is being charged. Switch $S_1$and diode D_1 are switched on, while the switch $S_2$and diode $D_2$are turned off. Additionally, a bidirectional converter moves excess power from the DC bus to the battery whenever there is an excess of energy generation.

3.6.2. Boost Mode

The bidirectional converter functions as a boost converter when the battery is being discharged. In this stage, the switch $S_2$and diode $D_2$are on, but switch $S_1$and diode $D_1$are off. In this mode, the converter moves energy from the battery to the DC bus. On the other hand, a bidirectional converter controls power flow and keeps the DC bus voltage stable in both charge and discharge modes when renewable energy output is insufficient.

4. Results and Discussion

The model is implemented using MATLAB/Simulink to analyze the performance in terms of efficiency, loss and control efficacy. The results obtained are presented and further evaluated via comparative analysis. Table 2 displays the specification of parameters for developed research.

Table 2. Parameter specification

Parameters	Values
PV System	
Open circuit voltage	37.25V
Short circuit current	8.95A
Number of cells connected in series	3
Number of cells connected in parallel	7
Voltage at MPP	36.63V
PV power rating	10 kW
Landsman Converter	
Switching Frequency	10KHz
L, L_1	4.7mH
C_1, C	22μF
Battery Specification	
Battery	100 Ah

4.1. Case 1: Varying Temperature and Irradiance

Figure 15 represents the solar panel and Landsman converter performance under varying temperatures and irradiance. The first two graphs show the solar panel temperature and irradiance waveform, from which it is notable that the solar temperature is maintained at 25°C for about 0.2 seconds, after which the temperature slightly rises to 35°C and is stabilized. Similarly, solar irradiance is maintained constant at 8

00 W/Sq-m for 0.4 seconds and then rises to 1000 W/Sq-m. The third and fourth graph depicts the Input DC voltage and current of the Landsman converter, where voltage initially begins at 100V and further rises beyond 100V and then remains constant, while the input DC current starts with certain fluctuation and is stabilized after 0.4 seconds respectively. Figure 16 denotes Landsman converter output current and voltage waveform, which implies voltage drops down to -600V and then is maintained at -600V with minor deviations. Whereas, the converter output current initially increases to -10A and further is maintained at -10A with uneven fluctuations.

Figure 17 represents input and output power, where both power rapidly rise beyond 10,000 W and then drop down to somewhere between 8000 W to 9000 W, further maintained at that particular power throughout the depicted time period with minor deviations from time to time, respectively.

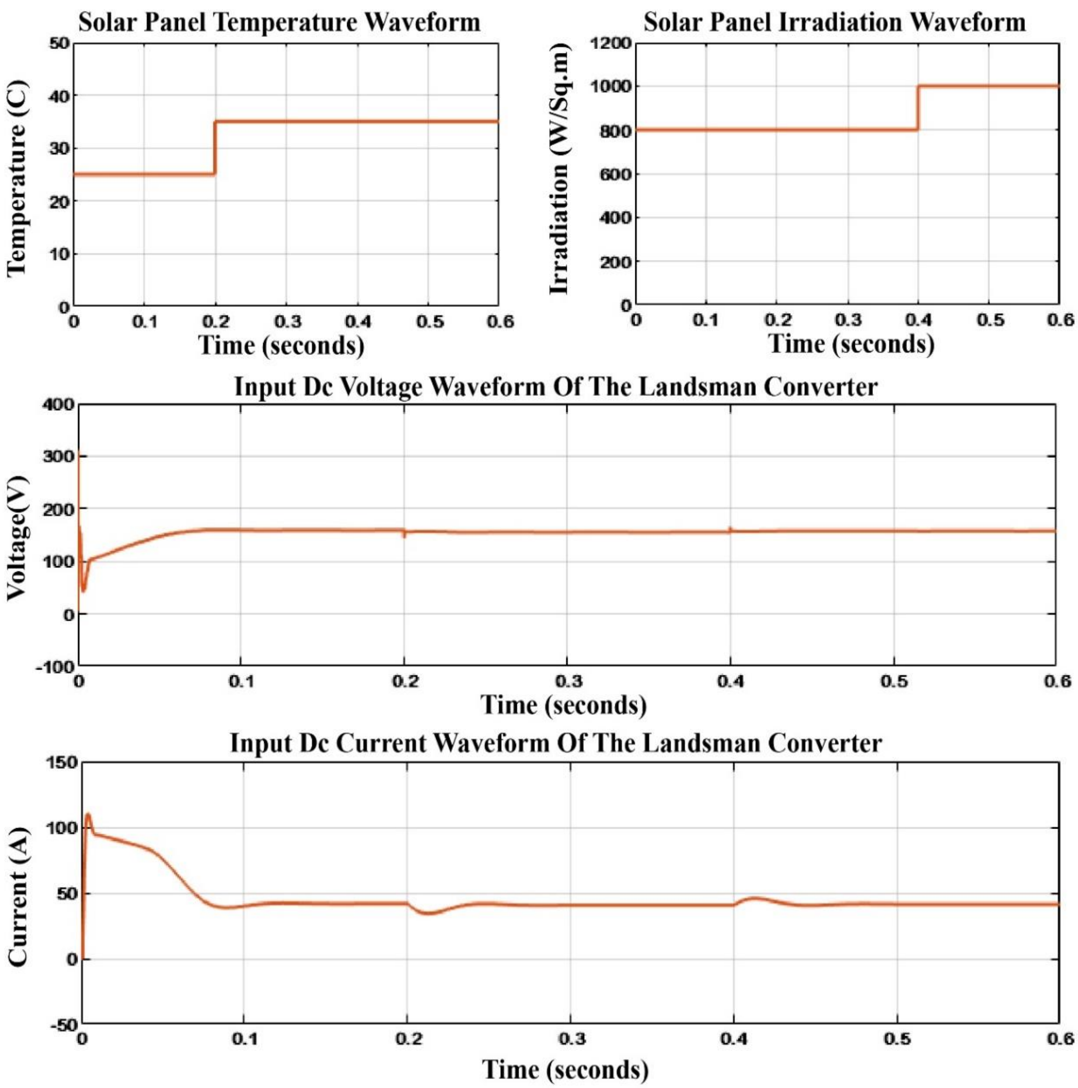

Fig. 15 Solar and converter waveform

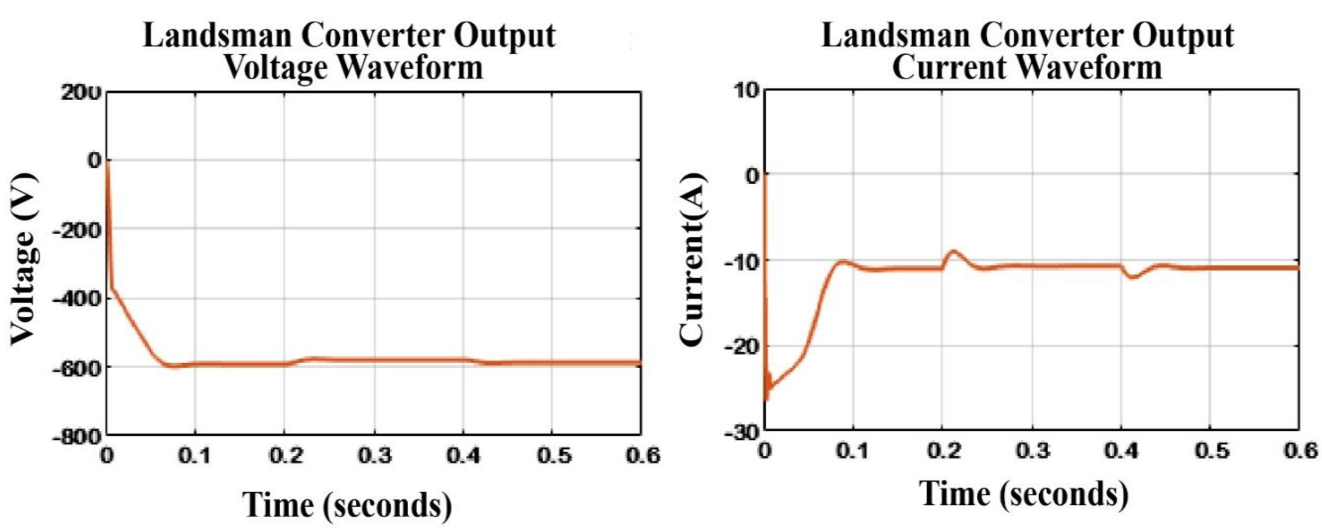

Fig. 16 Output current and voltage waveform

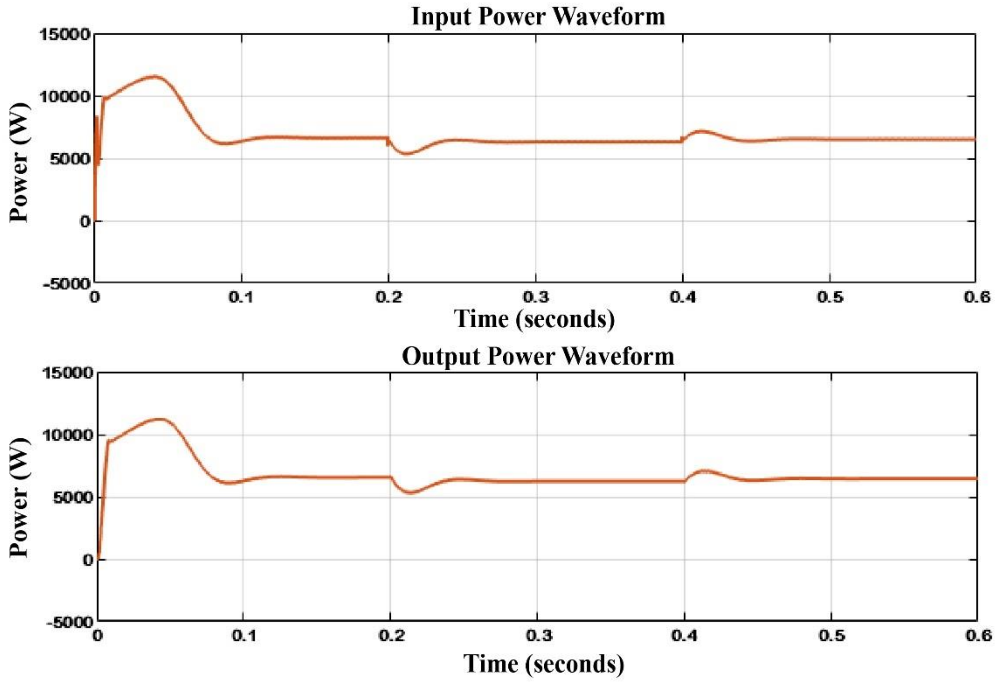

Fig. 17 Input and output power

4.2. Case 2: Constant Temperature and Irradiance

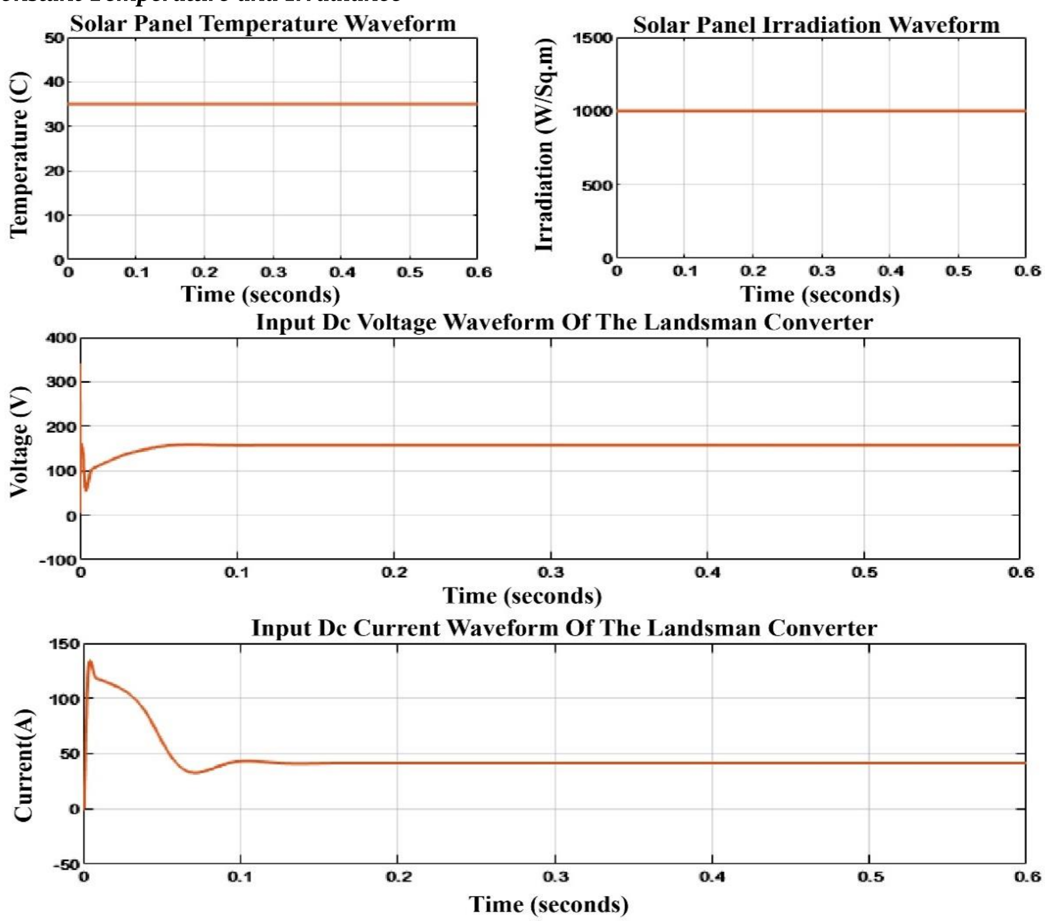

Fig. 18 Waveform of solar panel and converter

Figure 18 showcases the solar panel and converter performance. The first and second graph showcases the solar temperature and irradiance waveform maintained constant at 35°C and 1000 W/Sq-m through the time duration of 0.6 seconds. The third and fourth graph depicts the Landsman converter input DC voltage and current waveform, where voltage initially rises to 160V and stabilized with a smooth line, indicating zero fluctuations; likewise, the input DC current initially drops down below 50A and is maintained at 48 A through the depicted 0.6 seconds and the smooth line showcases, input current with null fluctuations respectively. Figure 19 demonstrates the Landsman converter output current and voltage waveform, where the output voltage initially drops down to -600V and is maintained stable through 0.6 seconds, and the converter current output initially increases beyond -10A and later stabilizes at -10A, respectively. Figure 20 represents the input and output power waveform, where both input and output power rapidly rises beyond 10,000 W and then drops down to 8000 W; after 0.1 seconds, both the powers are maintained at 8500 W throughout 0.6 seconds, indicating stable performance with consistent input and output power.

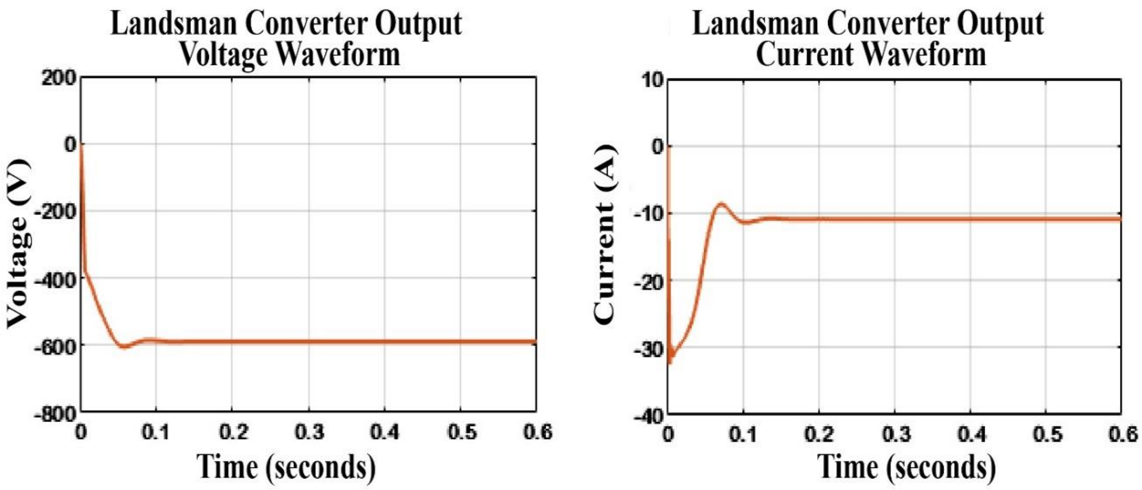

Fig. 19 Converter output current and voltage

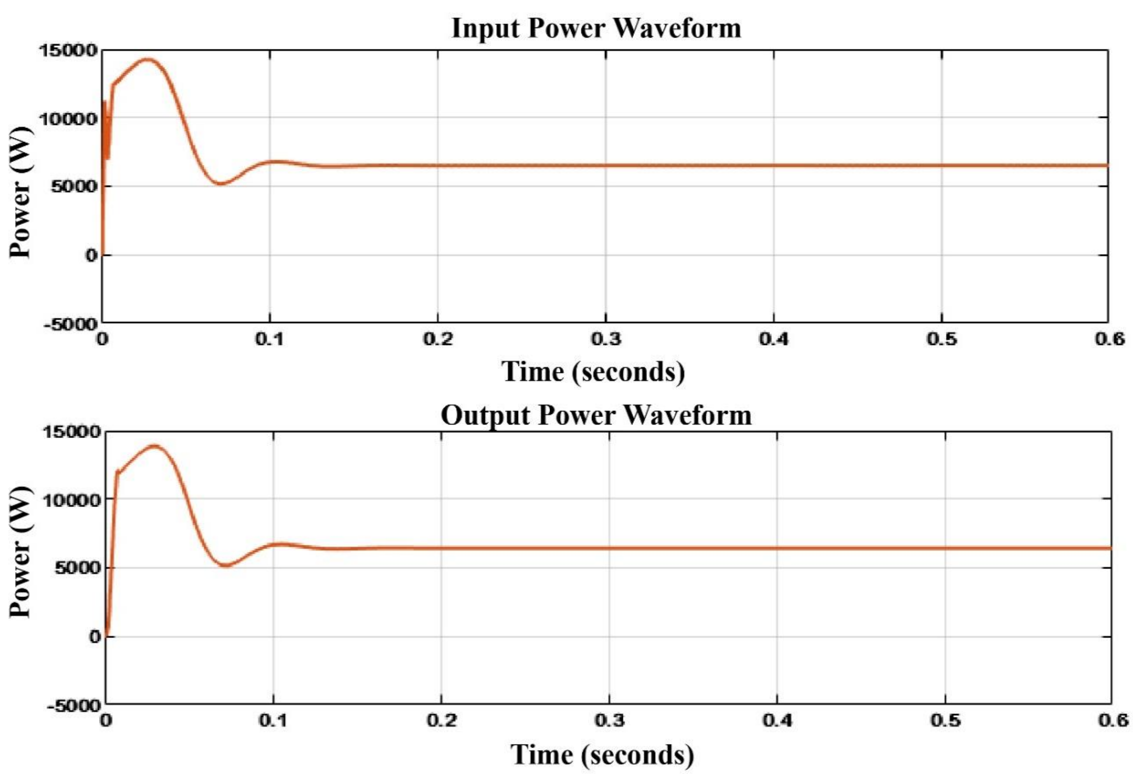

Fig. 20 power waveform

Figure 21 indicates the output voltage for FC and converter, in which the FC output voltage ranges between 0 to 390 V with initial fluctuations, which is further stabilized after 0.1 seconds, whereas the converter output voltage rapidly rises to 600 V and is maintained at 600V throughout the depicted time period of 0.6 seconds respectively.

Figure 22 depicts the supercapacitor output voltage waveform, in which the voltage initially rises beyond 200 V and then stabilizes at 230V, indicating enhanced charging and discharging performance. Figure 23 showcases the battery SOC performance, where all three graphs show smooth and fine lines indicating minimal or no fluctuations. The battery SOC is maintained at 70 %, the battery current depicts rapid increase and decrease, then is kept constant at 0, while the battery voltage is maintained at 150 V throughout the time period of 0.6 seconds, indicating consistent and stable battery performance. Figure 24 denotes the waveform of the BLDC motor; the first graph depicts the BLDC motor current, which is maintained at 0; the second graph depicts the BLDC motor back EMF, which progressively increases and is maintained between ±100 V; the third graph depicts the BLDC speed, which gradually increases to 4000 RPM and then stabilized. Finally, the last graph showcases the BLDC torque, which gradually decreases and then remains at 0.

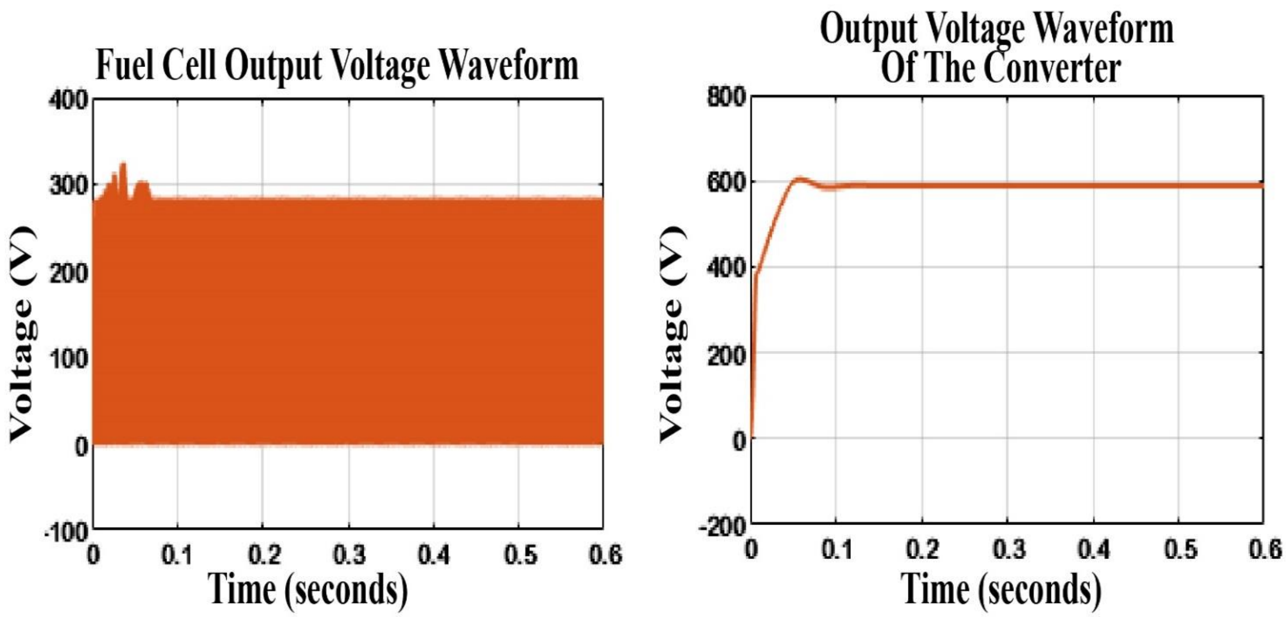

Fig. 21 Output voltage waveform

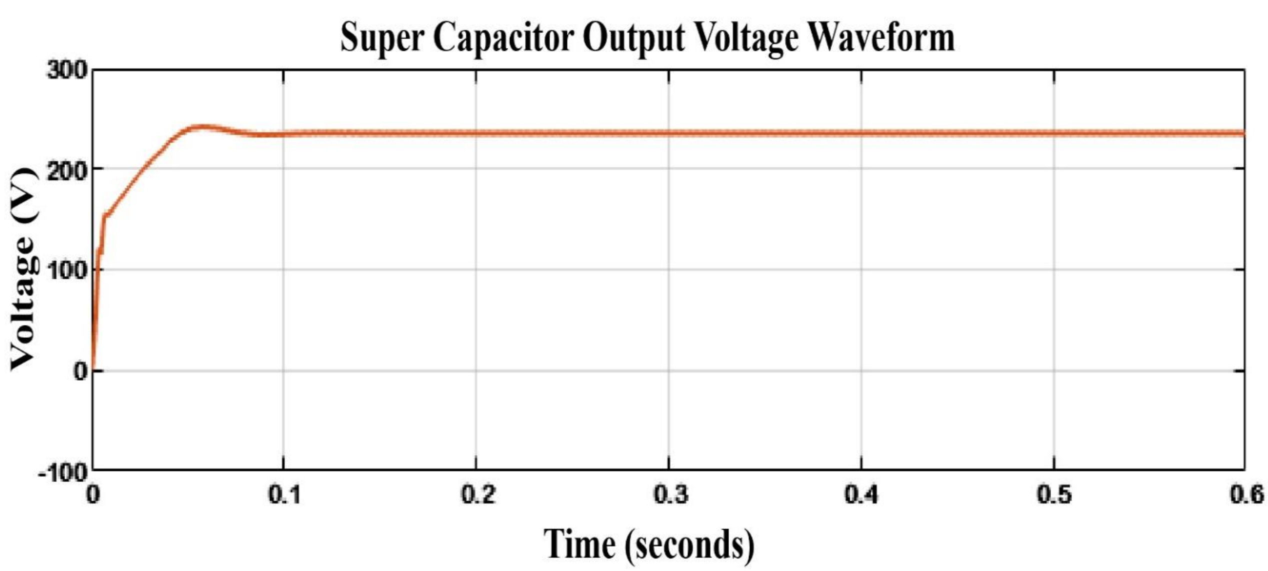

Fig. 22 Output voltage of supercapacitor

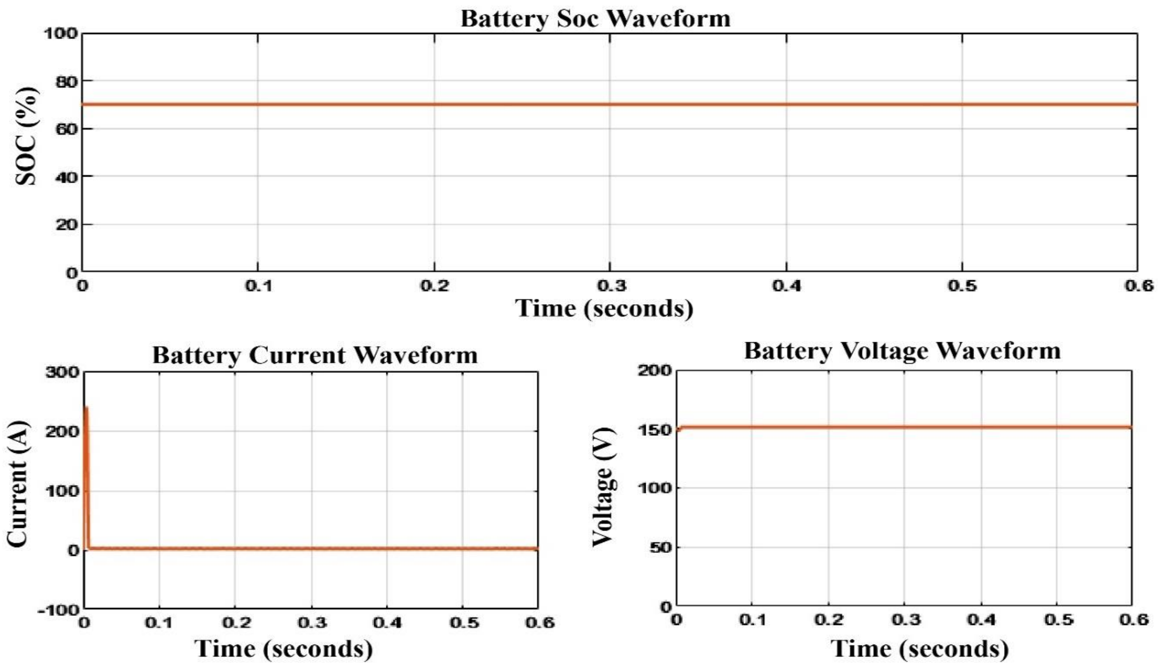

Fig. 23 Battery performance

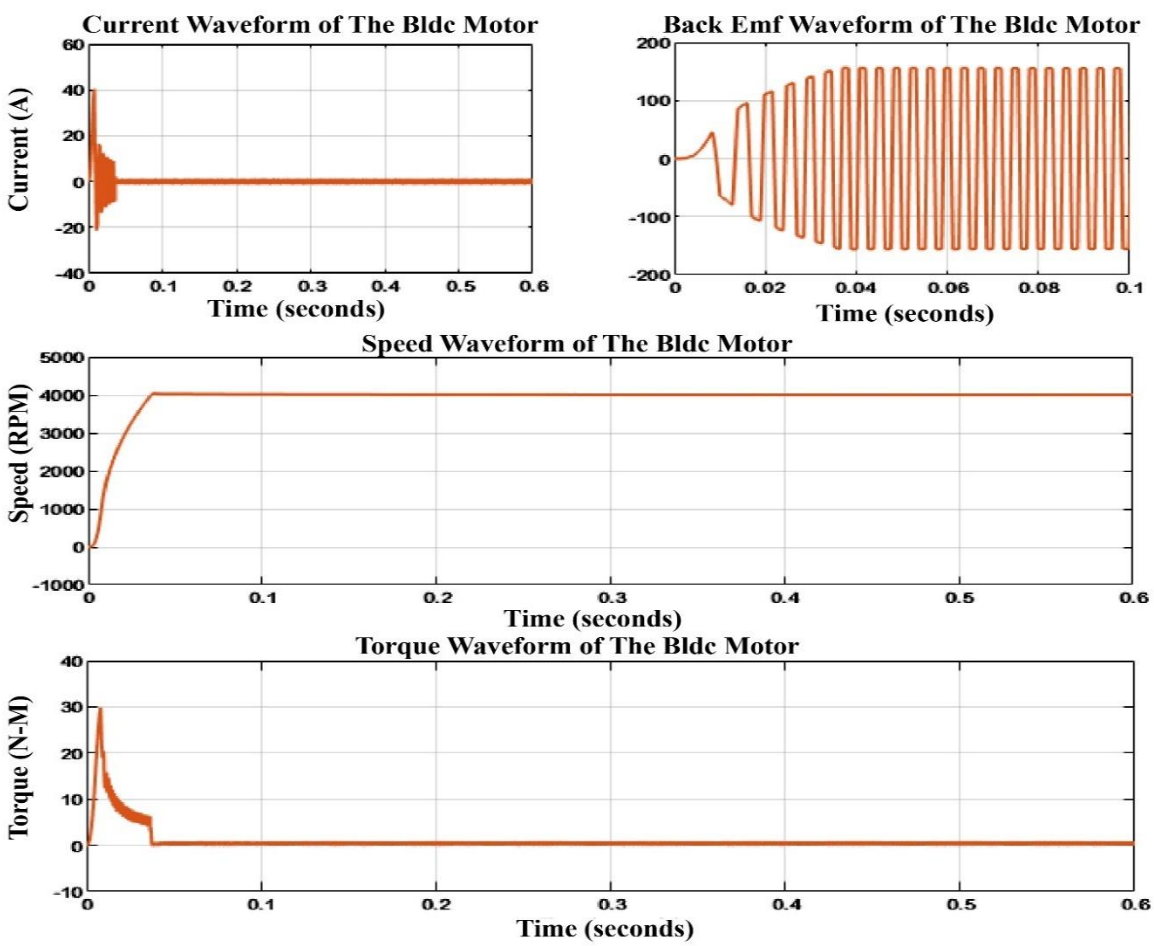

Fig. 24 BLDC motor performance waveform

4.3. Case 3: 0.5nm Load Applied At 0.3 Sec

Figure 25 demonstrates the waveform for speed and torque, where speed gradually increases and then maintains at 4000 RPM through the entire time duration, While torque gradually decreases and then remains at 0 and after 0.3 seconds shows minor deviation, indicating steady-state system functioning.

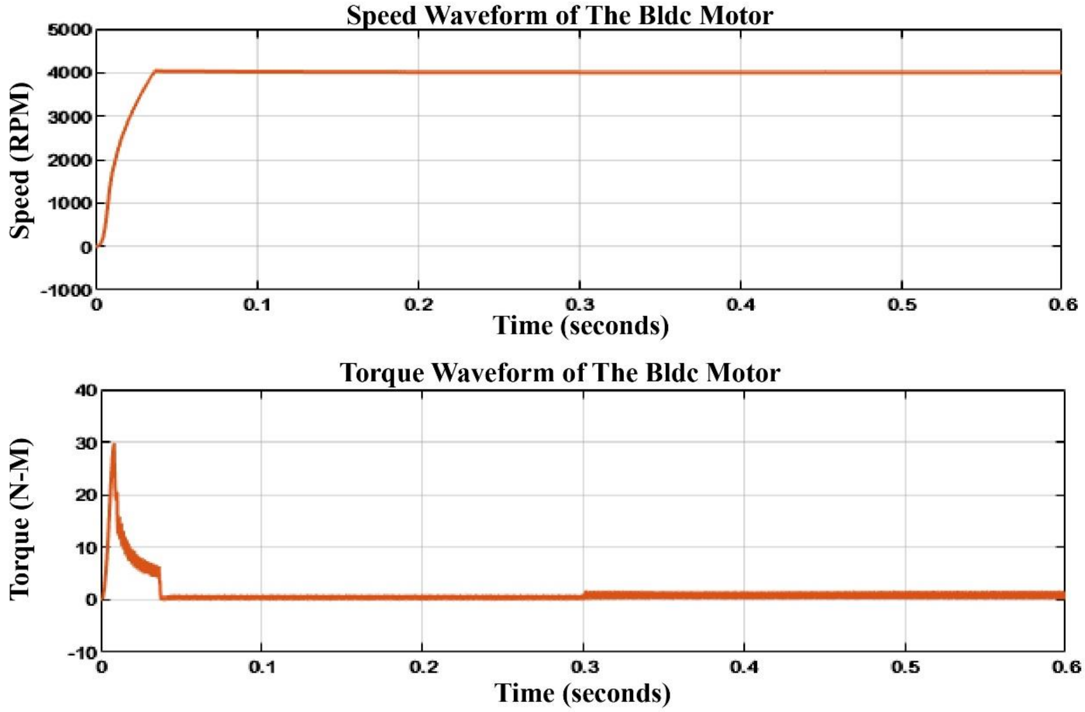

Fig. 25 Speed and torque waveform

4.4. Case 4: 1nm Load Applied At 0.3 Sec

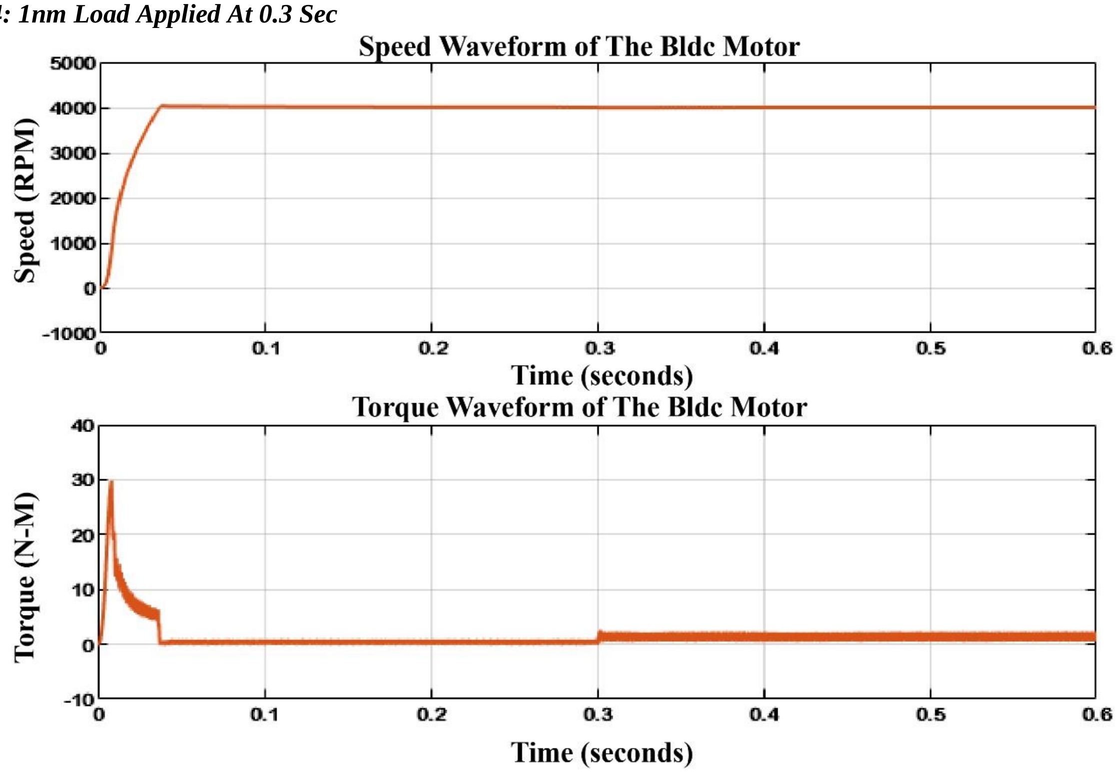

Fig. 26 BLDC motor speed and torque

Figure 26 represents the motor speed and torque; the first plot showcases that the motor speed progressively rises to 4000 RPM and is maintained at that particular speed throughout the depicted time duration of 0.6 Seconds, while the motor torque gradually drops down and then stays at 0 and after 0.3 seconds shows slight variations respectively. Figure 27 denotes the THD output indicating a value of 2.83%, which in turn proves improved power quality with reduced effect of harmonics on the BLDC motor. Figure 28 denotes the comparison of converter performance between the proposed Landsman converter and conventional Non-isolated High gain DC-DC converter [1]; from the above-showcased chart, it is visible that the proposed converter attains reduced switching loss of 1.12, diode conduction of 1.67 and capacitor loss of 0.23 when compared to the other conventional converter which attained higher losses respectively, referring to improved performance efficiency of the proposed converter over conventional converter, thereby making more reliable and effective. Figure 29 refers to the efficiency comparison between various converters such as Cuk [25], Boost [26], KY integrated SEPIC [27], Cascaded Boost Luo [28] and Proposed Landsman converter. All the other conventional converter showcases reduced efficiency of 94%, 96.59%, 96%, and 97%, while the proposed converter depicts a higher efficiency of 98%, indicating optimum performance with improved power conversion.

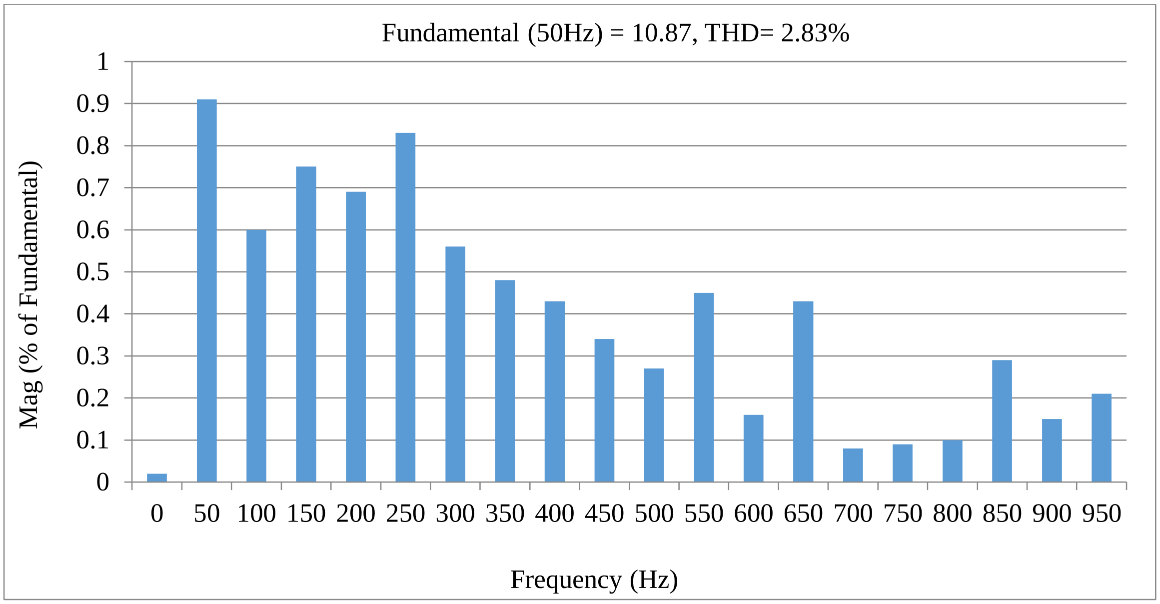

Fig. 27 THD output

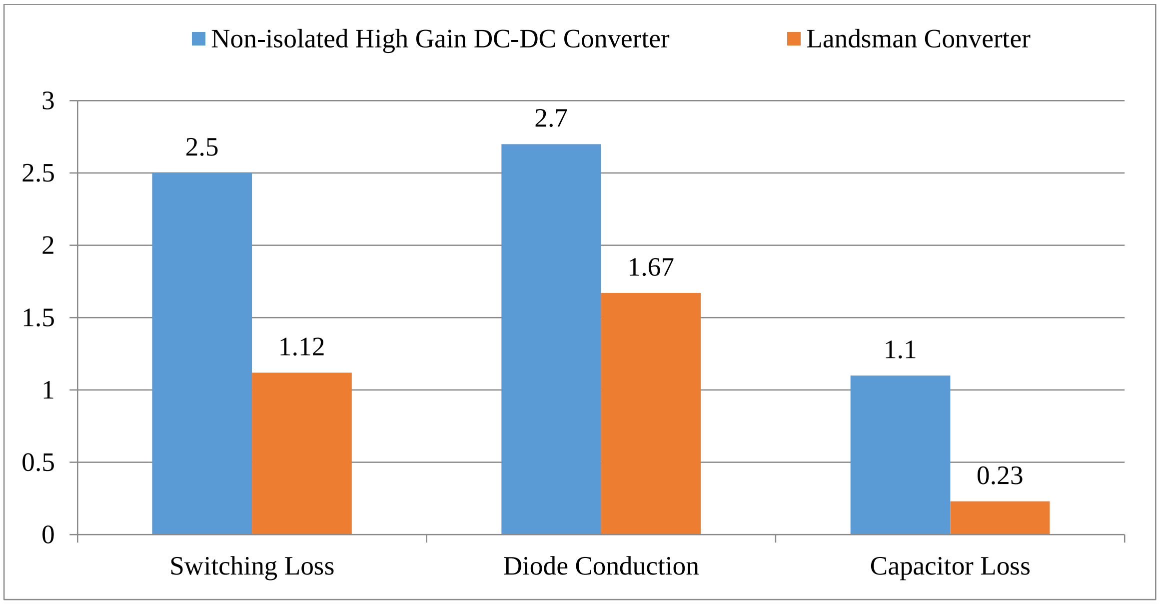

Fig. 28 Comparison of landsman converter performance

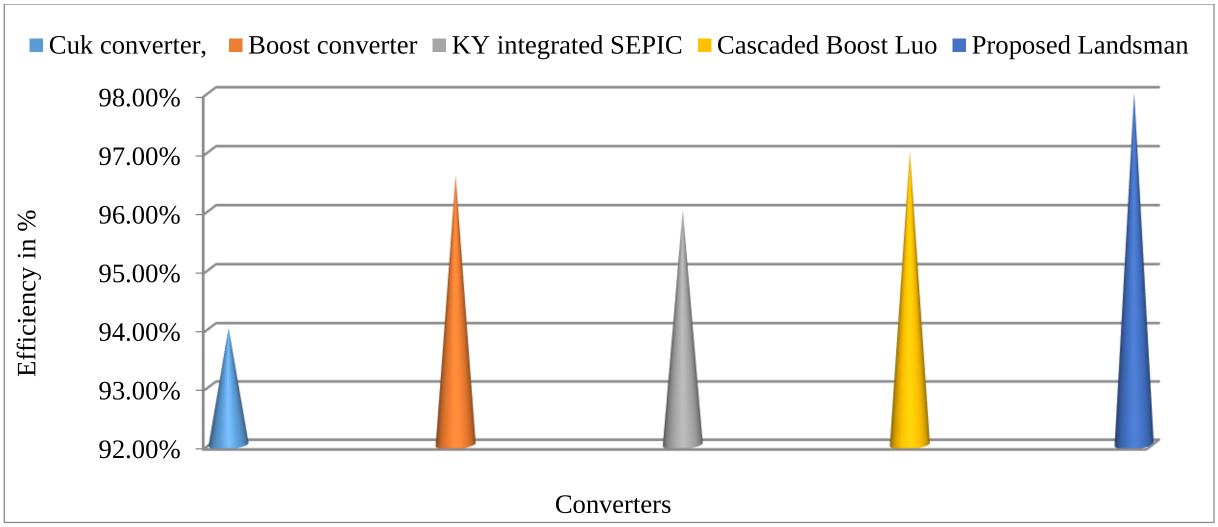

Fig. 29 Efficiency comparison

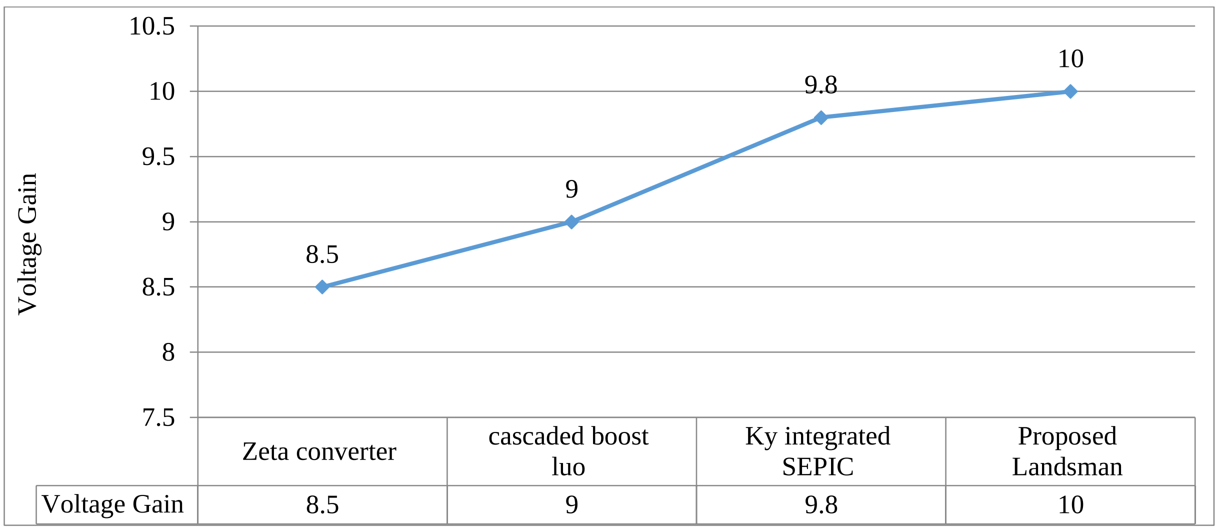

Fig. 30 Voltage gain

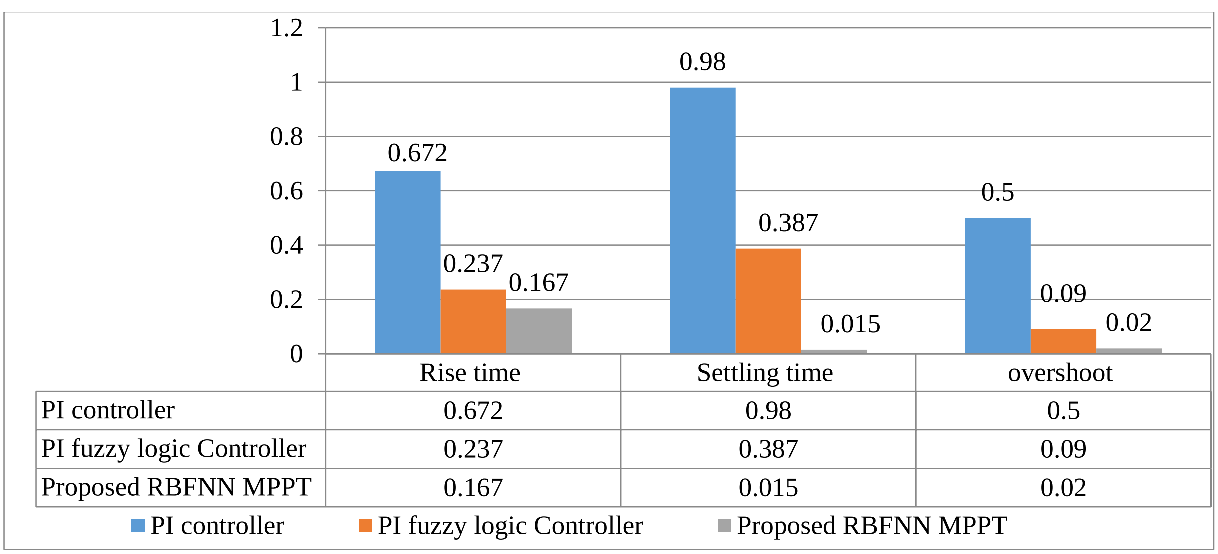

Fig. 31 Comparison of control approaches

Table 3. Comparison of BLDC with brushed motor

Parameter	Brushed Motor	BLDC Motor
Torque (Nm)	10-30Nm	20-50Nm
Speed (rpm)	1500	4000
Lifespan (hours)	1000-5000	10,000-50,000

Figure 30 implies the voltage gain comparison between conventional zeta [29], cascaded boost Luo [28], KY integrated SEPIC [27] and proposed converter to determine the performance efficacy of the proposed landsman converter. The Landsman converter attained a higher gain of 10, while the other converter attained a slightly reduced voltage gain, indicating the enhanced voltage regulating capability of the Landsman converter. Figure 31 indicates the comparison of control approaches such as PI controller [18] and PI Fuzzy logic controller [4] with the proposed RBFNN-based MPPT controller. The proposed control topology showcases a reduced rise time of 0.167, settling time of 0.015 and overshoot of 0.02 when compared to [4, 18], implying that the proposed RBFNN control approach attains rapid dynamic responses and improved stability.

Table 3 denotes the comparison of the BLDC motor with the Brushed motor. Compared with existing works, the proposed system offers superior performance owing to improved power conversion efficiency and intelligent control approaches. The Landsman converter exhibits reduced losses due to the optimized topology for improving energy transfer efficiency. Its enhanced voltage regulation ability increases efficiency and maintains the system's stability. Also, the MPPT controller outperforms other ones in literature due to its adaptive and self-learning ability, resulting in faster dynamic response.

4.5. Real-Time Validation of the Work

Considering practical validation, the Landsman converter demands an accurate selection of components for stable operation. Also, thermal management has to be taken into account when adopting cooling mechanisms. The MPPT controller needs a real-time microcontroller with the ability to handle fast data processing. Prototype testing has to be performed to assess system response, energy conversion efficiency and transient performance. Considering these factors, this system can be implemented for real-time EV applications.

5. Conclusion

The development of the proposed system utilizing HRES-based power sources, effective energy storage units, and better power control management addresses the issues related to sustainable and reliable EV performance. The integration of PV and FC provides a consistent and sustainable power supply to meet the energy requirements of the EV.

The deployment of a landsman converter assures a higher level of output voltage with increased gain and reduced losses. Furthermore, implementing an RBFNN-based MPPT controller demonstrates enhanced power control management with accurate and precise tracking ability. In addition to this, the utilization of battery and super-capacitor acts as an effective energy storage and retrieval units. Therefore, the overall system effectively improves EV performance in terms of increased reliability and efficiency with advanced energy management control.

The results obtained through the MATLAB/Simulink implementation validate that the proposed model attained a higher efficiency of 98% with reduced losses, thus ensuring improved system performance under varying circumstances. However, the suggested system can be improved further by introducing more advanced control approaches. Hence, hybrid control approaches can be included in future for improving the regulation of the entire system, thereby contributing to more optimized functioning of EV motors.

References

[1] A. Peer Mohamed et al., "Adaptive Maximum Power Extraction Technique in Fuel-Cell Integrated with Novel DC-DC Converter Topology for Low-Power Electric Vehicle Applications," *Engineering Science and Technology, an International Journal*, vol. 54, 2021. [CrossRef] [Google Scholar] [Publisher Link]

[2] Bhukya Laxman, Ramesh Gugulothu, and Surender Reddy Salkuti, "A Modified Particle Swarm Optimization-Based Adaptive Maximum Power Point Tracking Approach for Proton Exchange Membrane Fuel Cells," *Franklin Open,* vol. 8, 2024. [CrossRef] [Google Scholar] [Publisher Link]

[3] M. Komal Kumar et al., "Enhanced Energy Management System for Hybrid Solar and Fuel Cell-Based Electric Vehicle Charging Stations Using ANN Controllers," *African Journal of Biological Sciences*, vol. 6, no. 10, pp. 3991-3999, 2024. [Publisher Link]

[4] Yamina Jouili et al., "Adaptive Controller PI-Fuzzy Logic Speed for Brushless DC Motor Drive Supplied by PEMFC Cell Optimized by P&O," *International Journal on Applied Physics and Engineering*, vol. 23, pp. 76-92, 2023. [CrossRef] [Google Scholar] [Publisher Link]

[5] Nicu Bizon, and Phatiphat Thounthong, "Multi-Objective Energy Management Strategy for PV/FC Hybrid Power Systems," *Electronics,* vol. 10, no. 14, 2021. [CrossRef] [Google Scholar] [Publisher Link]

[6] K.S. Kavin, and P. Subha Karuvelam, "PV-Based Grid Interactive Pmbldc Electric Vehicle with High Gain Interleaved DC-DC Sepic Converter," *IETE Journal of Research,* vol. 69, no. 7, pp. 4791-4805, 2023. [CrossRef] [Google Scholar] [Publisher Link]

[7] Awab Baqar, Mamadou Baïlo Camara, and Brayima Dakyo, "Supercapacitors Fast Ageing Control in Residential Microgrid Based Photovoltaic/Fuel Cell/Electric Vehicle Charging Station," *Energies,* vol. 16, no. 13, pp. 1-25, 2023. [CrossRef] [Google Scholar] [Publisher Link]

[8] G. Mathesh, Raju Saravanakumar, and Rohit Salgotra, "Novel Machine Learning Control for Power Management Using an Instantaneous Reference Current in Multiple-Source-Fed Electric Vehicles," *Energies,* vol. 17, no. 11, pp. 1-28, 2024. [CrossRef] [Google Scholar] [Publisher Link]

[9] Izhar Ul Haq et al., "Neural Network-Based Adaptive Global Sliding Mode MPPT Controller Design for Stand-Alone Photovoltaic Systems," *Plos One,* vol. 17, no. 1, 2022. [CrossRef] [Google Scholar] [Publisher Link]

[10] Badreddine Kanouni et al., "Advanced Efficient Energy Management Strategy Based on State Machine Control for Multi-Sources PV-PEMFC-Batteries System," *Scientific Reports,* vol. 14, no. 1, 2024. [CrossRef] [Google Scholar] [Publisher Link]

[11] K.R.M. Vijaya Chandrakala et al., "Implementation of High Step up Converter Using RBFN MPPT Controller for Fuel Cell Based Electric Vehicle Application," *Scientific Reports,* vol. 14, no. 1, 2024. [CrossRef] [Google Scholar] [Publisher Link]

[12] Aissa Benhammou et al., "Accurate and Efficient Energy Management System of Fuel Cell/Battery/Supercapacitor/AC and DC Generators Hybrid Electric Vehicles," *Sustainability*, vol. 15, no. 13, pp. 1-27, 2023. [CrossRef] [Google Scholar] [Publisher Link]

[13] B. Raja Sekhar Reddy, V.C. Veera Reddy, and M. Vijaya Kumar, "Hybrid DC-DC Converter with Artificial Intelligence Based MPPT Algorithm for FC-EV", *Journal of Scientific & Industrial Research / Electronics Information and Communication Technology*, vol. 82, no. 5, 2023. [CrossRef] [Google Scholar] [Publisher Link]

[14] Yamina Jouili et al., "Self-Adaptive PI-FLC for BLDC Motor Speed Supplied by PEM Fuel Cell Stack Optimized by MPPT," *Arabian Journal for Science and Engineering,* vol. 49, no. 5, pp. 6487-6503, 2024. [CrossRef] [Google Scholar] [Publisher Link]

[15] Mahmoud F. Elmorshedy et al., "Energy Management of Hybrid DC Microgrid with Different Levels of DC Bus Voltage for Various Load Types," *Energies,* vol. 16, no. 14, pp. 1-32, 2023. [CrossRef] [Google Scholar] [Publisher Link]

[16] K. S. Kavin et al., "A Novel KSK Converter with Machine Learning MPPT for PV Applications", *Electric Power Components and Systems*, pp. 1-19, 2024. [CrossRef] [Google Scholar] [Publisher Link]

[17] Satyajeet Sahoo et al., "Artificial Deep Neural Network in Hybrid PV System for Controlling the Power Management," *International Journal of Photoenergy*, no. 1, pp. 1-12, 2022. [CrossRef] [Google Scholar] [Publisher Link]

[18] Muhammad Rafaqat Ishaque et al., "Fuzzy Logic-Based Duty Cycle Controller for the Energy Management System of Hybrid Electric Vehicles with Hybrid Energy Storage System," *Applied Sciences,* vol. 11, no. 7, pp. 1-29, 2021. [CrossRef] [Google Scholar] [Publisher Link]

[19] K.S. Kavin et al., "Improved BRBFNN-Based MPPT Algorithm for Coupled Inductor KSK Converter for Sustainable PV System Applications," *Electrical Engineering,* 2025. [CrossRef] [Google Scholar] [Publisher Link]

[20] Nabil A. Ahmed et al., "Soft Switching Multiphase Interleaved Boost Converter with High Voltage Gain for EV Applications," *IEEE Access*, vol. 10, pp. 27698-27716, 2022. [CrossRef] [Google Scholar] [Publisher Link]

[21] Shaik Reddi Khasim, C. Dhanamjayulu, and S.M. Muyeen, "A Single Inductor Multi-Port Power Converter for Electric Vehicle Applications," *IEEE Access*, vol. 11, pp. 3367-3385, 2023. [CrossRef] [Google Scholar] [Publisher Link]

[22] Wiljan Vermeer, Gautham Ram Chandra Mouli, and Pavol Bauer, "Optimal Sizing And Control of a PV-EV-BES Charging System Including Primary Frequency Control and Component Degradation," *IEEE Open Journal of the Industrial Electronics Society*, vol. 3, pp. 236-251, 2022. [CrossRef] [Google Scholar] [Publisher Link]

[23] Galiveeti Hemakumar Reddy et al., "Simultaneous Placement of Multiple Rooftop Solar PV Integrated Electric Vehicle Charging Stations for Reliability Benefits," *IEEE Access*, vol. 11, pp. 130788-130801, 2023. [CrossRef] [Google Scholar] [Publisher Link]

[24] Jun-Hyeok Heo, Jun-Kyu Kang, and Jin Hur, "Verification of Shaft Voltage Reduction Effect using Layered-Shield in EV Traction Motors," *IEEE Access*, vol. 12, pp. 136825-136836, 2024. [CrossRef] [Google Scholar] [Publisher Link]

[25] Ahmed Darwish, "A Bidirectional Modular CUK-Based Power Converter for Shore Power Renewable Energy Systems," *Energies,* vol. 16, no. 1, pp. 1-28, 2022. [CrossRef] [Google Scholar] [Publisher Link]

[26] Akhil Raj, and R.P. Praveen, "Highly Efficient DC-DC Boost Converter Implemented with Improved MPPT Algorithm for Utility Level Photovoltaic Applications," *Ain Shams Engineering Journal*, vol. 13, no. 3, 2022. [CrossRef] [Google Scholar] [Publisher Link]

[27] G. Vasumathi, V. Jayalakshmi, and K. Sakthivel, "Efficiency Analysis of Grid Tied PV System with KY Integrated Sepic Converter," *Measurement: Sensors,* vol. 27, 2023. [CrossRef] [Google Scholar] [Publisher Link]

[28] Hossein Gholizadeh et al., "Design and Implementation a Single-Switch Step-Up DC-DC Converter Based on Cascaded Boost and Luo Converters," *Energies,* vol. 14, no. 12, pp. 1-18, 2021. [CrossRef] [Google Scholar] [Publisher Link]

[29] Padala Lakshmi Santosh Kumar Reddy et al., "A Non-Isolated Hybrid Zeta Converter with a High Voltage Gain and Reduced Size of Components," *Electronics*, vol. 11, no. 3, pp. 1-17, 2022. [CrossRef] [Google Scholar] [Publisher Link]